

# All-in-One Conditioning for Text-to-Image Synthesis

Hirunima Jayasekara<sup>1</sup>, Chuong Huynh<sup>1</sup> Yixuan Ren<sup>1</sup>

Christabel Acquaye<sup>1</sup> Abhinav Shrivastava<sup>1</sup>

<sup>1</sup>University of Maryland, College Park

## Abstract

Accurate interpretation and visual representation of complex prompts involving multiple objects, attributes, and spatial relationships is a critical challenge in text-to-image synthesis. Despite recent advancements in generating photorealistic outputs, current models often struggle with maintaining semantic fidelity and structural coherence when processing intricate textual inputs. We propose a novel approach that grounds text-to-image synthesis within the framework of scene graph structures, aiming to enhance the compositional abilities of existing models. Eventhough, prior approaches have attempted to address this by using pre-defined layout maps derived from prompts, such rigid constraints often limit compositional flexibility and diversity. In contrast, we introduce a zero-shot, scene graph-based conditioning mechanism that generates soft visual guidance during inference. At the core of our method is the Attribute-Size-Quantity-Location (ASQL) Conditioner, which produces visual conditions via a lightweight language model and guides diffusion-based generation through inference-time optimization. This enables the model to maintain text-image alignment while supporting lightweight, coherent, and diverse image synthesis.

## Introduction

Recent advancements in text-to-image synthesis have demonstrated improved accuracy and diversity in generating high quality outputs (Saharia et al. 2022; Rombach et al. 2022; Ramesh et al. 2022a; Balaji et al. 2022). However, current models exhibit significant limitations when processing complex prompts that incorporate multiple objects and attributes with complex spatial relationships. Which leads to synthesized images manifesting inconsistencies with the provided text prompts, including the conflation or complete omission of specified objects, attributes, and spatial arrangements (Tong, Jones, and Steinhardt 2024; Bakr et al. 2023; Chen, Laina, and Vedaldi 2024; Phung, Ge, and Huang 2024).

This observation expose a critical gap in the semantic understanding and compositional abilities of existing text-to-image models. While these systems excel at generating individual elements with high fidelity, they struggle to accurately interpret and visually represent the holistic scene described in more elaborate textual inputs (Tong, Jones, and Steinhardt 2024). Although this behavior is partially inherited from large vision-language models (Yuksekgonul et al. 2022; Tong et al. 2024) such as CLIP (Radford et al. 2021), which

are employed to decode textual input, by introducing sophisticated mechanisms for parsing and maintaining the relational integrity of complex prompt elements may facilitate the embedding of the prompt's comprehensive conceptualization into the image generation process.

Prior work has attempted to address this challenge by constraining image generation through the use of pre-drawn layout maps derived from input prompts (Phung, Ge, and Huang 2024; Li et al. 2023b). However, this approach presents several limitations. Primarily, it restricts the placement and dimensioning of objects to the confines of the generated layout, potentially compromising the flexibility and naturalness of the resulting compositions. Furthermore, this method often results in a notable lack of diversity among the generated images. The separate generation of layouts significantly constrains the potential for dynamic adjustments to the spatial structure during the diffusion process, thereby limiting the model's ability to adapt and refine the image composition in response to emerging details or contextual nuances. This rigidity in layout generation may inadvertently constrain the model's capacity to produce varied and contextually appropriate visual representations.

Our work mitigate this problem by grounding the text-to-image synthesis with intermediate conditioning. Specifically, we impose an explicit representation on the text prompt using scene graphs and leverage the structuredness it provides to perform noise latent restructuring. The use of scene graphs in image generation pipelines has been previously explored in the literature. However, existing approaches have predominantly employed scene graphs either to modulate text embeddings derived from the input prompt (Feng et al. 2022; Shen et al. 2024; Feng et al. 2023) or to train auxiliary modules that enforce strict visual constraints for layout guidance(Farshad et al. 2023; Wang et al. 2024). We leverage scene graphs to generate soft visual conditions in a zero-shot manner, subsequently use them to guide the image generation process. To achieve this, we propose Attribute-Size-Quantity-Location(ASQL) Conditioner, which performs two core functions, 1) generating visual conditions via a light weight Large Language Models(LLMs) 2) leveraging the conditions to perform inference-time diffusion optimization(Chefer et al. 2023). We ensure that these conditions comprehensively capture all visual aspects of an image, while adhering to the constraints specified in the textual conditions, thereby en-

abling the model to generate images with coherence and flexibility.

Through extensive experiments we show that by plugin ASQL Conditioner, our method can significantly improve over state-of-the-art models. Our key contributions are as follows:

- We propose a zero-shot, robust image generation pipeline that incorporates scene graph-based conditioning to enhance spatial comprehension and diversify generation outcomes, complemented by a novel regime of loss functions that model spatial, size, quantity, and attribute relationships through soft region allocations based on fuzzy logic, enabling more natural object interactions.
- We introduce a lightweight conditioning framework to generate visual guidance constraints through multi-turn prompting using light weight low-parameter LLMs.
- Experimental results demonstrate that the proposed method achieves state-of-the-art performance on three standard benchmark datasets, highlighting its effectiveness and robustness across diverse evaluation scenarios.

## Related Work

**Image Generation.** Image generation has progressed significantly from VAEs (Kingma and Welling 2014) and GANs (Goodfellow et al. 2020) to the current dominance of diffusion models (Ho, Jain, and Abbeel 2020; Rombach et al. 2021; Ramesh et al. 2022b; Peebles and Xie 2023). Diffusion models generate images by reversing a noise process, offering high fidelity and controllability. Ho *et al.* (Ho, Jain, and Abbeel 2020) introduced the basic framework, while Song *et al.* (Song et al. 2021) extended it with a score-based approach. Rombach *et al.* (Rombach et al. 2021) improved efficiency by operating in latent space rather than pixel space. More recently, PixArt- $\alpha$  (Chen et al. 2023) demonstrated that a transformer-based diffusion architecture can scale text-to-image generation to high resolutions while maintaining strong semantic alignment.

**Conditional Diffusion Models.** Conditional diffusion models allow generation to be guided by labels, text, or layouts (Nichol et al. 2022; Ho 2022; Rombach et al. 2021). Several approaches enhance layout control by fine-tuning on layout-image pairs (Avrahami et al. 2023; Li et al. 2023b), or modifying sampling (Balaji et al. 2022; Bansal et al. 2023; Chen, Laina, and Vedaldi 2024). Mixture-of-Diffusion (Jiménez 2023) and MultiDiffusion (Kumari et al. 2023) denoise local regions and fuse results, while Dense Diffusion (Kim et al. 2023) alters attention maps directly. Recent works (Phung, Ge, and Huang 2024; Feng et al. 2024) use LLM-generated layouts but require costly inference and impose rigid constraints, leading to less natural outputs.

Others modify cross-attention maps at test time (Chefer et al. 2023; Phung, Ge, and Huang 2024; Zhang, Yu, and Wu 2024; Sueyoshi and Matsubara 2024). Attend-and-Excite (Chefer et al. 2023) updates latents using attention, while EBAMA (Zhang, Yu, and Wu 2024) and Predicated Diffusion (Sueyoshi and Matsubara 2024) introduce object-attribute consistency losses. We propose a hybrid strategy: identify plausible regions per entity and apply soft spatial

guidance, avoiding rigid layouts while maintaining alignment and diversity.

Existing approaches (Xu et al. 2024a; Wu et al. 2023; Feng et al. 2024) rely on extensive training procedures to align scene representations with image generation, often requiring task-specific architectures (Feng et al. 2024; Farshad et al. 2023) and supervised data. In contrast, our proposed method is training-free, leveraging pre-trained diffusion models without additional fine-tuning or task-specific retraining, which significantly reduces computational cost while maintaining competitive performance.

**LLMs for Visual Understanding.** LLMs have shown promise in spatial reasoning (Xu et al. 2024b; Wei et al. 2022; Yamada et al. 2023). CoT prompting (Wei et al. 2022) improves performance on spatial tasks, while recent studies (Xu et al. 2024b; Yamada et al. 2023) show that even small models can reason about basic spatial relations. These findings motivate our use of lightweight LLMs for extracting soft spatial constraints from text.

**Scene Graph Generation.** Scene graphs represent objects and their relationships in a structured format, aiding tasks like image retrieval (Schuster et al. 2015; Pham et al. 2024; Johnson et al. 2015) and caption evaluation (Yang et al. 2023). While their use in image generation is limited (Johnson, Gupta, and Fei-Fei 2018; Herzig et al. 2020), recent work has explored generating scene graphs from text (Choi, Heo, and Zhang 2022; Zhong et al. 2021; Wang, Beck, and Cohn 2019), enabling structured guidance from unstructured input.

## Method

In this section, we describe our approach to improve the attribute-size-quantity-location (ASQL) awareness of text-to-image generation pipeline. We first start with the preliminaries of foundations in Sec. , followed by the overview of our solution in Sec. . The details of ASQL conditioning are explained in the last two sections.

## Preliminaries

**Text-to-image Diffusion Models.** Text-to-image diffusion models rely on an iterative denoising process starting from a random Gaussian noise  $x_T \sim \mathcal{N}(0, 1)$ . At each denoising timestep  $t$ , a model (*e.g.*, UNet) predicts the noise residual  $\epsilon_t = \phi(x_t; \mathbf{c})$  given the noisy input  $x_t$  and a conditioning signal  $\mathbf{c}$ . In text-to-image generation, the condition  $\mathbf{c} = f_t(\mathbf{w}) \in \mathbb{R}^{n \times e}$  corresponds to text embeddings obtained from a text encoder  $f_t$  (*e.g.*, CLIP) applied to the input text  $\mathbf{w} = (w_1, \dots, w_n)$ . Text guidance is incorporated into the denoising process via a cross-attention mechanism, where the *key*  $\mathbf{K} \in \mathbb{R}^{n \times d}$  and *value*  $\mathbf{V} \in \mathbb{R}^{n \times d}$  are computed from  $\mathbf{c}$  using learned linear projections. Given a set of queries  $\mathbf{Q} \in \mathbb{R}^{hw \times d}$  derived from the image feature map of size  $h \times w$ , the cross-attention map  $A_t \in [0, 1]^{hw \times n}$  at timestep  $t$  is computed as:

$$A_t = \text{softmax} \left( \frac{\mathbf{Q} \mathbf{K}^\top}{\sqrt{d}} \right) \quad (1)$$

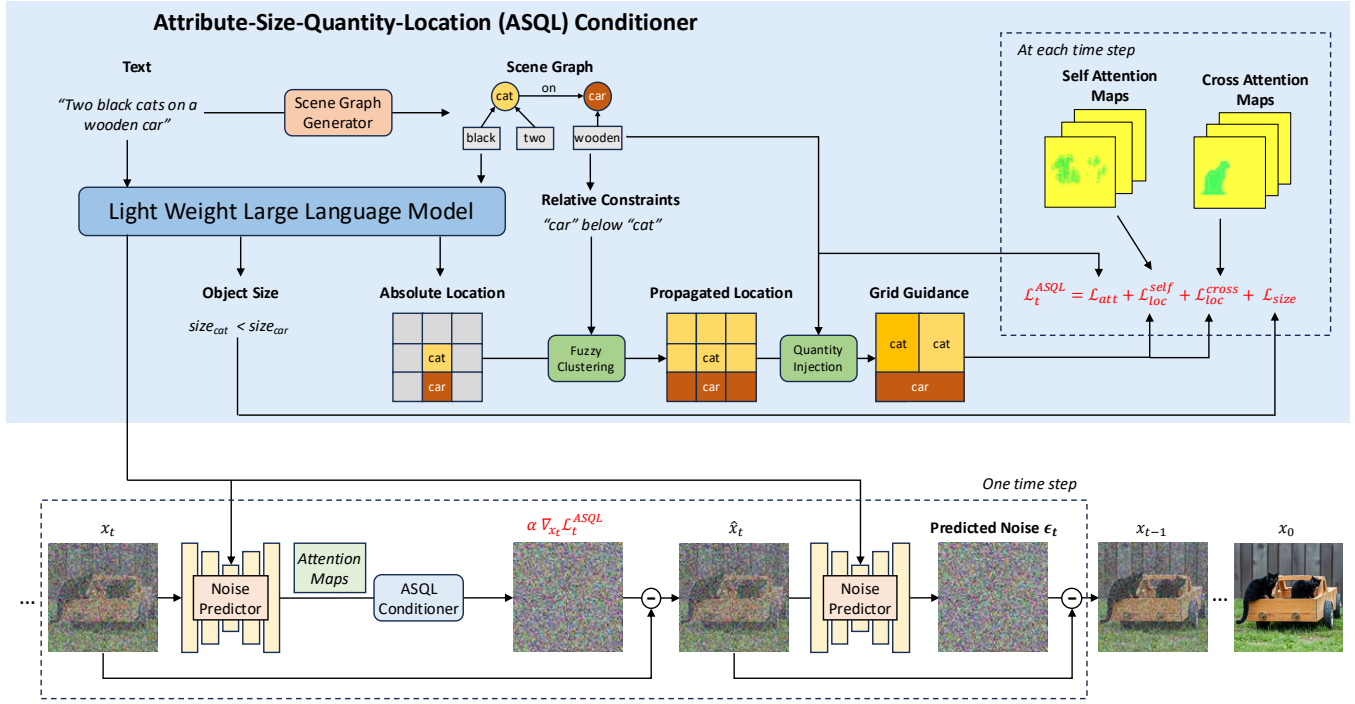


Figure 1: **Our ASQL Conditioning Pipeline.** Given a text condition, we generate intermediate conditions to control the image denoising process at each time step. All properties (size, quantity, attributes) of each entity and relationships between entities are considered to achieve the best result.

which captures the association between each word token  $w_i$  and spatial locations in the image feature map.

**Inference-time Diffusion Optimization.** To enhance text-image alignment, many methods employ inference-time optimization. Given a noisy input  $x_t$  at timestep  $t$  and an inference-time loss  $\mathcal{L}_t$ , the model performs a forward and backward pass through the noise predictor  $\phi$  to compute the gradient  $\nabla_{x_t} \mathcal{L}_t$ . The input is then updated as  $\hat{x}_t = x_t - \alpha \nabla_{x_t} \mathcal{L}_t$ , where  $\alpha$  is a controlling strength. The noise predictor then refines its prediction based on the updated input  $\hat{x}_t$ . The loss  $\mathcal{L}_t$  often incorporates attention maps  $A_t$  to guide the spatial alignment between the text tokens and image regions. The process is illustrated in the below part of Fig. 1.

**Scene Graphs.** Scene graphs represent images or captions as graphs, where each entity is a node and the relationships between entities are edges. Each node may also contain sub-nodes that represent the entity’s attributes. Let  $S = (V, E)$  be a scene graph, where  $V$  is the set of entities and  $E$  is the set of relationships. Each entity  $v_i = (o, q, a_1, \dots, a_k)$  consists of an entity name  $o$ , the quantity  $q$  and a list of corresponding attributes  $a_j$ .

## Overall Framework

Our proposed pipeline focuses on improving the text-following capacity of text-to-image diffusion models using CLIP text encoder. Following practical approaches (Chefer

et al. 2023; Phung, Ge, and Huang 2024), we define a new inference-time loss  $\mathcal{L}^{ASQL}$  to modify the input at each time step. Large Language Models (LLM), which has good ability in instruction understanding, help generating guidance in different forms which covers all main challenges about relationship and attribute object binding in text-to-image generation: Attribute, Size, Quantity, Location.

We leverage LLMs to generate guidance at inference-time. This guidance is then reused at each denoising time step  $t$  to compute  $\mathcal{L}_t^{ASQL}$  with the attention maps  $A_t$ .

## ASQL Guidance Generation

The top part of the Fig. 1 illustrates the pipeline to generate augmented information that adhere the text-to-image generation process. LLMs joins to construct the guidance from the original text and its corresponding scene graph. To further improve the guidance, especially for location and quantity, we propose to enhance the LLM’s guidance to have a more accurate grid as a layout constraint.

**Augmented Guidance Generation.** The LLMs takes the caption and its scene graph representation as input and generate two intermediate information pieces to support the conditioning process:

*Object Size* is a sorted list of objects in size increasing order  $\bar{V} = \{v_i | \text{size}(v_i) < \text{size}(v_j) \forall i < j\}$ . It joins to control the relative size between objects.

*Absolute Location* is a possible grid location for a given entity

in an image grid  $G = \{u_{xy} \in [0, |V|]\}$  where  $u_{xy}$  indicates entity id at row  $y$ -th and column  $x$ -th. Each nonzero value indicates the initial location for the entity.

*Relative Constraints* contains the relative constraints between objects in both horizontal and vertical directions. While some text explicitly contains this information, others (e.g., “cat rides a motorbike”) does not have. We utilize the relationships derived from each scene graphs to extract these information to improve the visual guidance. For every ordered entity pairs  $\{(v_i, v_j) | i \neq j\}$ , we compute the vertical and horizontal relation  $\mathbf{v}_{ij} \in \{\text{ABOVE, SAME, BELOW}\}$ ,  $\mathbf{h}_{ij} \in \{\text{LEFT, SAME, RIGHT}\}$

While the Object Size is directly used to control the image synthesis (explained in Sec. ), the remaining factors contribute to the enhancement process to construct the complete grid guidance. Details regarding prompts and output formats are in the supplementary material.

**Grid Guidance Enhancement.** As illustrated in the top part of Fig. 1, the pipeline includes two steps: (1) *Fuzzy Clustering* to assign each cell to an entity and (2) *Quantity Injection* to divide the entity region to  $q$  sub-regions.

In Fuzzy Clustering, we need to assign each cell  $(x, y)$  to the entity with the highest membership:

$$u_{xy} = \arg \max_{v_j \in V} \mu(v_j, (x, y)) \quad (2)$$

where  $\mu(v_j, (x, y))$  is the aggregated membership score indicating how suitable it is for entity  $v_j$  to occupy cell  $(x, y)$ . This membership score is derived by combining the relative spatial constraints between  $v_j$  and all other entities  $\{v_i | i \neq j\} \in V$ , using  $\mathbf{v}, \mathbf{h}$  relations. A cell is considered a candidate for  $v_j$  only if it satisfies all the directional constraints in the fuzzy rule base.

In details, for each cell  $(x, y)$ , the feasibility of placing  $v_j$  with respect to  $v_i$  is:

$$\mu_{ij}(x, y) = \mu_{\text{range}_x, ij}(x) \cdot \mu_{\text{range}_y, ij}(y) \in \{0, 1\}. \quad (3)$$

where

$$\mu_{\text{range}_x, ij}(x) = \begin{cases} 1, & \mathbf{h}_{ij} = \text{RIGHT} \wedge x > x_i \\ 1, & \mathbf{h}_{ij} = \text{LEFT} \wedge x < x_i \\ 1, & \mathbf{h}_{ij} = \text{SAME} \wedge x = x_i \\ 0, & \text{otherwise} \end{cases} \quad (4)$$

$$\mu_{\text{range}_y, ij}(y) = \begin{cases} 1, & \mathbf{v}_{ij} = \text{ABOVE} \wedge y < y_i \\ 1, & \mathbf{v}_{ij} = \text{BELOW} \wedge y > y_i \\ 1, & \mathbf{v}_{ij} = \text{SAME} \wedge y = y_i \\ 0, & \text{otherwise} \end{cases} \quad (5)$$

To compute  $\mu(v_j, (p, q))$ , starting with the all-ones matrix  $\mathbf{M}^{(j)}(x, y) = 1$ , for every other entity  $v_i$ , we update:

$$\mathbf{M}^{(j)}(x, y) \leftarrow \mathbf{M}^{(j)}(x, y) \cdot \mu_{ij}(x, y). \quad (6)$$

Because the values are binary, the product is simply the logical AND of all pair-wise masks. After looping over all  $i \neq j$  we obtain the final membership

$$\mu(v_j, (x, y)) = \mathbf{M}^{(j)}(x, y) \in \{0, 1\} \quad (7)$$

Inorder to incorporate quantity information from the scene graph into the grid  $G$  we leverage the quantity annotations provided in the graph. For each entity with  $q$  quantities, we divide the respective region into equal  $q$  sub-regions, as showed in Fig. 1.

### ASQL Guidance Loss

Following previous works (Chefer et al. 2023; Phung, Ge, and Huang 2024), we compute the  $\mathcal{L}^{\text{ASQL}}$  between the attention score and the guidance obtained from previous section. Instead of using softmax function, we use the score after the sigmoid as:

$$\tilde{A}_t = \sigma \left( \beta \frac{\mathbf{QK}^\top}{\sqrt{d}} \right) \quad (8)$$

where  $\beta = 100$ . The attention still captures the association between each word token and spatial locations but is independent. To simplify, we remove the time step  $t$  from the notation of  $\tilde{A}$

**Attribute Guidance Loss.** In order to reduce the attribute leakage between entities, we control the attention map between each entity with each corresponding attributes as the attribute loss  $\mathcal{L}_{\text{att}}$ :

$$\mathcal{L}_{\text{att}} = \frac{1}{|V|} \sum_v^V \frac{1}{k} \sum_a^v \text{BCE} \left( \tilde{A}^v, \tilde{A}^a \right) + \eta \tilde{A}^a (1 - \tilde{A}^v) \quad (9)$$

where  $\tilde{A}^o, \tilde{A}^a$  is corresponding attention map of object name and attribute in each entity, BCE is the binary cross-entropy loss, and  $\eta$  is the regularization parameter.

**Size Guidance Loss.** To control the size of objects, from the Object Size entity set  $\bar{V}$ , we compute the pair-wise loss between summation of attention maps of two consecutive object:

$$\mathcal{L}_{\text{size}} = \frac{1}{|V|} \sum_i^{|V|-1} \max \left( 0, \|\tilde{A}^i\| - \|\tilde{A}^{i+1}\| \right) \quad (10)$$

where  $\tilde{A}^i$  is the corresponding attention map for the  $i$ -th entity in  $\bar{V}$  and  $\|\cdot\|$  denotes the summation of all entries in the matrix.

**Location Guidance Loss.** The location-based penalization comprises two components. First, we calculate a location loss  $\mathcal{L}_{\text{loc}}^{\text{cross}}$  derived from cross-attention maps. We employ grid guidance in the form of binary masks  $G$ . To mitigate the effects of hard masking, we apply a Euclidean distance transform (Huang and Mitchell 2002) to each entity mask corresponding to entity  $v$ , resulting a softened representation denoted as  $\bar{G}^v$ . To ensure holistic representation of each object,  $\mathcal{L}_{\text{loc}}^{\text{cross}}$  is computed using the 2-D Dice loss(Sudre et al. 2017) for each entity  $v$ :

$$\mathcal{L}_{\text{loc}}^{\text{cross}} = \sum_e^V 1 - \frac{2 \|\tilde{A}^v \cdot \bar{G}^v\|}{\|\tilde{A}^v\| + \|\bar{G}^v\|} \quad (11)$$

Secondly, the self-attention-based location loss  $\mathcal{L}_{\text{loc}}^{\text{self}}$  is computed. Similarly, we compute a Euclidean distance-transformed 3D mask  $\hat{G}^v$  for each entity  $v$  using  $G$ .

Table 1: Performance on all three benchmarks HRS, T2I-CompBench and GenEval. Our achieves the best performance on most metrics.  $\dagger, \star, \diamond$  indicates the base as SDv1.4, PixArt- $\alpha$  and SDv2.1 respectively.

Method	HRS				T2I-CompBench				GenEval				
	Count	Spatial	Size	Color	Color	Texture	Shape	Spatial	2-Obj	Count	Color	Position	Attribute
	F1 $\uparrow$	Acc $\uparrow$	Acc $\uparrow$	Acc $\uparrow$	BLIP $\uparrow$	BLIP $\uparrow$	BLIP $\uparrow$	Acc $\uparrow$					
CLIP Retrieval(Beaumont 2022)	-	-	-	-	-	-	-	-	0.22	0.37	0.62	0.03	0.00
Mini DALL-E (Dayma et al. 2021)	0.39	0.04	0.02	0.02	-	-	-	-	0.11	0.12	0.37	0.02	0.01
SDv1.4 (Rombach et al. 2022)	0.58	0.09	0.09	0.13	0.37	0.42	0.37	0.13	0.38	0.35	0.76	0.04	0.06
Attend-n-Excite $^\dagger$ (Chefer et al. 2023)	0.61	0.10	0.11	0.20	-	-	-	-	-	-	-	-	-
Ours $^\dagger$	0.51	0.21	0.16	0.14	0.41	0.44	0.39	0.20	0.40	0.31	0.74	0.16	0.09
PixArt- $\alpha$ (Chen et al. 2023)	0.55	0.19	0.16	0.18	0.39	0.45	0.36	0.18	0.47	0.42	0.78	0.08	0.12
Ours $^*$	0.55	0.21	0.18	0.20	0.41	0.46	0.39	0.21	0.51	0.42	0.80	0.12	0.08
SDv2.1 (Rombach et al. 2022)	0.56	0.17	0.13	0.22	0.57	0.50	0.45	0.17	0.51	<b>0.44</b>	<b>0.85</b>	0.07	0.17
Composable $^\diamond$ (Liu et al. 2022)	-	-	-	-	0.41	0.37	0.33	0.08	-	-	-	-	-
Structured $^\diamond$ (Feng et al. 2022)	-	-	-	-	0.50	0.49	0.42	0.14	-	-	-	-	-
Attend-n-Excite $^\diamond$ (Chefer et al. 2023)	0.63	0.26	0.14	0.31	0.64	0.60	0.45	0.15	0.65	0.38	0.80	0.12	0.21
EBAMA $^\dagger$ (Zhang, Yu, and Wu 2024)	0.63	0.27	0.12	0.32	-	-	-	-	0.67	0.36	0.84	0.12	0.23
Ours $^\diamond$	<b>0.66</b>	<b>0.28</b>	<b>0.17</b>	<b>0.37</b>	<b>0.69</b>	<b>0.63</b>	<b>0.52</b>	<b>0.27</b>	<b>0.69</b>	0.40	0.76	<b>0.41</b>	<b>0.24</b>

where,  $\hat{G}^v$  is extended along the channel dimension and multiplied by its flattened counterpart. This operation accentuates spatial regions likely to contain the object, facilitating more precise localization. Subsequently, a 3D Dice loss is computed between the self-attention output  $\hat{A}$  and the computed mask. Pseudocode for the mask generation process is provided in the supplementary material.

$$\mathcal{L}_{\text{loc}}^{\text{self}} = \sum_e^V \sum_s^{H \times W} 1 - \frac{2\|\hat{A} \cdot \hat{G}^v\|}{\|\hat{A}\| + \|\hat{G}^v\|} \quad (12)$$

The final  $\mathcal{L}_t^{\text{ASQL}}$  loss at timestep  $t$  is computed as a weighted combination of all three losses.

$$\mathcal{L}_t^{\text{ASQL}} = \lambda_1 \mathcal{L}_{\text{att}} + \lambda_2 \mathcal{L}_{\text{size}} + \lambda_3 \mathcal{L}_{\text{loc}}^{\text{cross}} + \lambda_4 \mathcal{L}_{\text{loc}}^{\text{self}} \quad (13)$$

where  $\lambda_1, \lambda_2, \lambda_3, \lambda_4$  are hyper-parameters.

## Experiments

### Baselines and Benchmarks

**Baselines.** We compare our proposed pipeline with other baselines with stable diffusion versions: Attend-and-Excite (Chefer et al. 2023), EBAMA (Zhang, Yu, and Wu 2024). We refer to several baselines models while evaluating the capacity of the new model. We compare the proposed model with models without region suggestions given, Stable Diffusion (Rombach et al. 2021) (1.4V, 2.1V) and Attend-and-excite (Chefer et al. 2023), EBAMA (Zhang, Yu, and Wu 2024) and multi diffusion(Kumari et al. 2023).

**Evaluation Metrics.** We utilize HRS (Bakr et al. 2023), GenEval (Ghosh, Hajishirzi, and Schmidt 2023) and T2I-CompBench (Huang et al. 2023) benchmarks on evaluating

the proposed model on several categories: accuracy, robustness, and generalization. For HRS, we focus on the accuracy improvements, we consider four categories, counting, spatial, color and size compositions. Each sample consists of prompt, object’s name and corresponding category used for evaluation. T2I-CompBench deploys a BLIP-VQA(Li et al. 2023a) model to evaluate the color, position, and attribute binding for generated images while deploying an object detector to compute spatial accuracy. Similarly, GenEval employs a object detector followed by a color classifier to identify two object relations, counting, color, position(spatial) and attribute binding.

**Implementation.** We conduct all the experiments on one NVIDIA RTX A6000 GPU with batch size of 1. The proposed pipeline is built on the public official implementation of Attend-and-Excite (Chefer et al. 2023). For scene graph generator, we utilize our own scene graph-LLM, finetuning Llama-3.1-Tulu-3-8B (Lambert et al. 2024) on FACTUAL (Li et al. 2023c) dataset. Performance of our new scene graph generator and finetuning details is in the supplementary material. We utilized Phi3-instruct(Abdin et al. 2024) as our light weight LLM. We followed the SD baseline for sampling which requires in 24 attention resolution for SD v2.1 and 16 attention resolution for SD v1.4. We sample the noise latent for 50 steps. Similarly, we used PixArt- $\alpha$  (Chen et al. 2023) sampling scheme with 64 attention resolution and 20 sampling steps to generate the final image. Empirical analysis on hyper-parameters for each pipeline can be found in the supplementary.

### Quantitative Results

Comparison on all benchmarks is shown in Table 1 with both base SD versions. In overall, we achieve the best score in

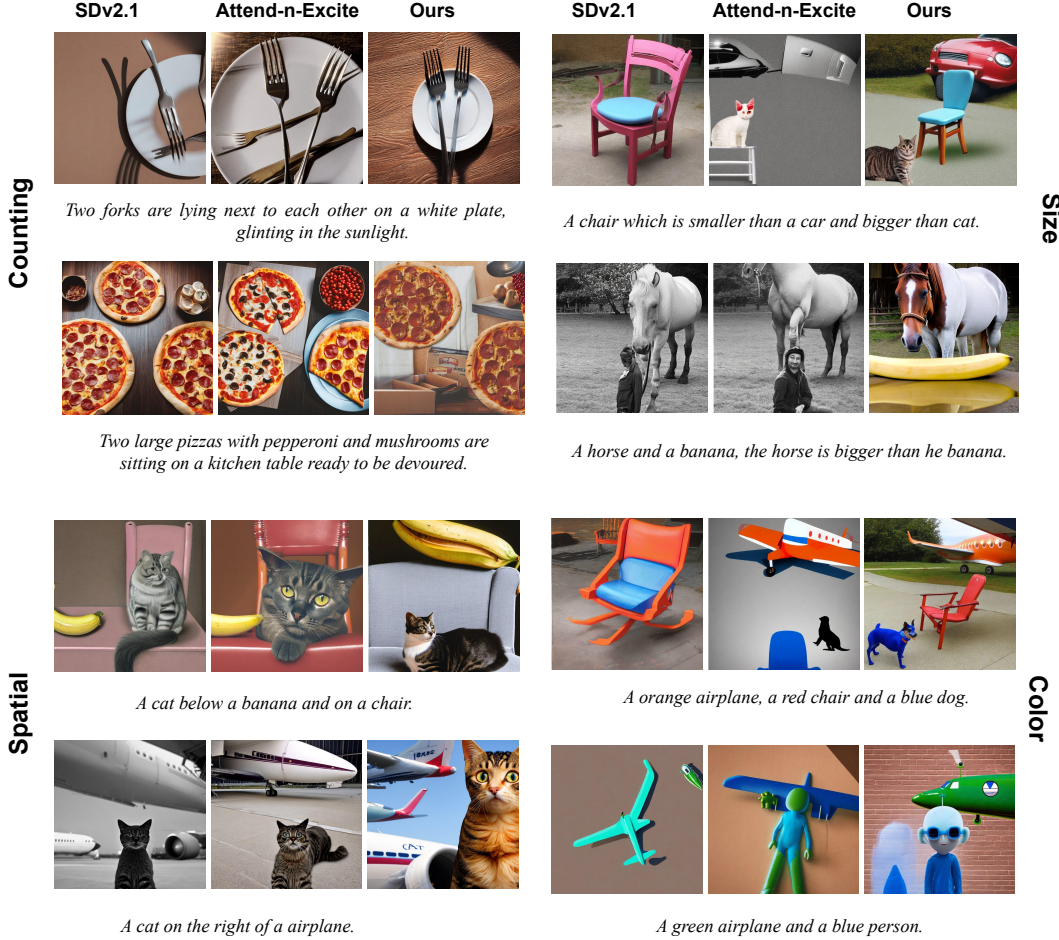


Figure 2: Qualitative results for proposed method. First two columns: images generated from baselines SDv2.1 and Attend-n-Excite with SDv2.1 base, Third column: image generated from proposed method.

most metrics with a large margin, proving the effectiveness of our solution. In HRS, the proposed method improves the F1 score by 3% and increases color accuracy by 5%. Additionally, it achieves a 1% performance gain in both size and spatial accuracy.

As shown in Table 1, Compared to the baselines, the proposed model yields a 5% and 7% increase in BLIP scores for color and shape, respectively, and a substantial 12% improvement in the spatial category.

Furthermore, the proposed model demonstrates significantly enhanced performance, achieving a 29% increase in accuracy for the position category on the GenEval benchmark. Additionally, the model yields accuracy gains of 2% and 1% in the two-objects and attributes categories, respectively. However, a decline in performance is observed for the counting and color categories, where as SDv2.1 outperforms latent modification methods.

## Qualitative Results

Figure 2 illustrates qualitative results of the proposed method. We evaluate the model on four sub categories. Namely, counting, spatial, color and size. We present three samples, one each from baseline models and proposed model where, Column 1: Stable Diffusion v2.1 , column 2: Attend and Excite with SDv2.1 base, column 3: proposed method. For each example, ground-truth prompt positioned at the bottom. Results of our model showcase the ability to bind attributes to respective objects while maintaining spatial consistency across the generated image.

## Ablation Experiments

We conduct several ablations on proposed method to illustrate the effectiveness and robustness of proposed modifications.

**Effect of Spatial Loss:** To assess the impact of the spatial loss, we evaluate the model using a combination of size and attribute losses, as presented in Table 2(4). The results indicate a significant decline in position accuracy when the spatial loss is omitted.

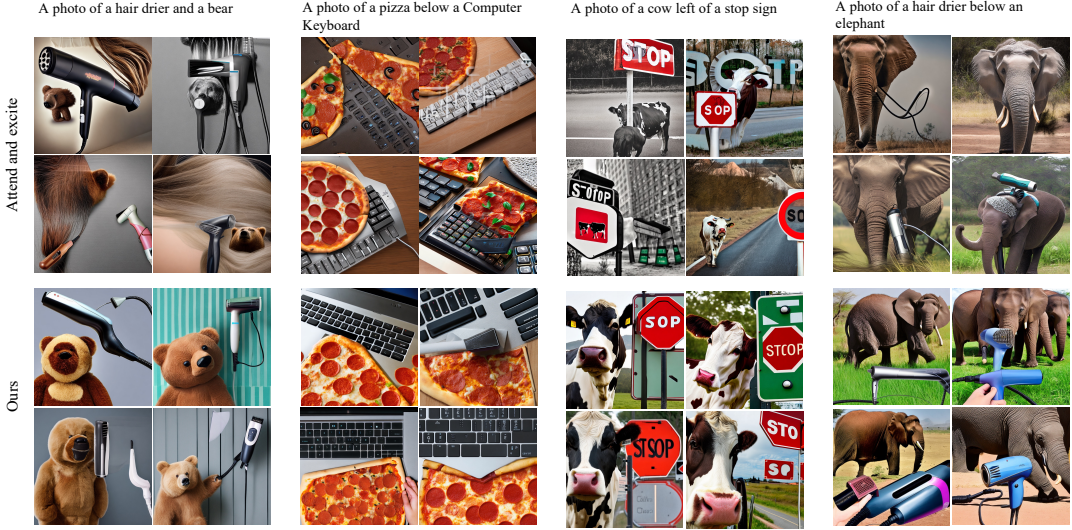


Figure 3: Qualitative results for proposed method. We compare our results on two objects and position with Attend-n-Excite with SDv2.1 base.

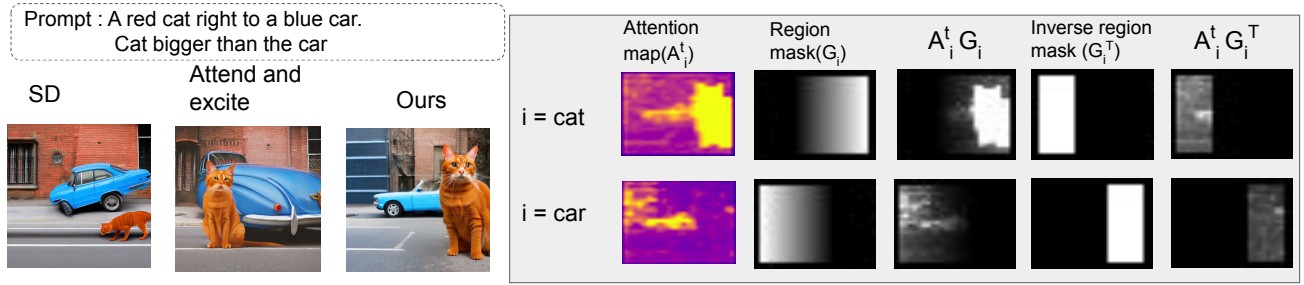


Figure 4: Example of Soft Region masking and effect of dice loss and size loss. First column shows the generated image from SD and Attend and excite. Second column illustrate the image generated with proposed pipeline.

Table 2: Ablation Experiments on GenEval benchmark. We systematically exclude each loss function and evaluate the model’s performance using the remaining components.

Effect	Two objects	Counting	Color	Position	Attribute Binding
(0) Baseline	0.69	0.40	0.76	0.41	0.24
(1) W/O LLM Region Suggestions	0.66	0.34	0.72	0.34	0.20
(2) Spatial Loss + Size Loss	0.66	0.39	0.74	0.40	0.20
(3) Spatial Loss + Attribute Loss	0.67	0.39	0.75	0.40	0.25
(4) Size Loss + Attribute Loss	0.69	0.37	0.74	0.35	0.23

**Effect of Size Loss:** To evaluate the contribution of the size loss, we assess the model’s performance using only the spatial and attribute losses. As shown in Table 2(3), this results in a decline in counting accuracy. While the size loss primarily ensures that the relative sizes of entities are preserved, it also influences entity presence by encouraging the model to maximize the spatial area allocated to each entity.

**Effect of Attribute Loss:** To assess the impact of the attribute loss, we evaluate the model using only the spatial and size

Table 3: Effect of different LLMs in ASQL Conditioner. We utilized smaller variation of Phi, Llama and Deep-seek to compute the visual constrains.

Method	Two objects	Counting	Color	Position	Attribute Binding
Phi3-mini-4k-instruct(Abdin et al. 2024)	0.69	0.40	0.76	0.41	0.25
Llama-3.1-8B-Instruct (Touvron et al. 2023)	0.43	0.35	0.75	0.35	0.17
DeepSeek-R1-Distill-Qwen-1.5B (Guo et al. 2025)	0.35	0.25	0.52	0.20	0.10

losses. As shown in Table 2(2), we can observe a drop in attribute accuracy.

**Effect of Soft Region Masking:** Figure 4 illustrate the effect of soft region masking where First column shows the generated image from SD and Attend and excite. Second column illustrate the image generated with proposed pipeline. Top image of the second column is generated with dice loss while the bottom image is generated with size loss. Last Five columns denotes the extracted attention maps for each entity ( $A_i^t$ ), soft region mask for each object ( $G_i$ ), region-entity attention maps ( $A_i^t G_i$ ), inverse region mask ( $G_i^T$ ) and



**Figure 5: Failed Generations.** First two columns: images generated overly literal manner, Last three columns: entity is either absent or too complex to be fully captured by the text prompt.

restrictive regions for each entity ( $A_i^t G_i^T$ ) respectively.

**Effect of LLM usage:** Proposed method relies on visual information constraints generated by a LLM. Consequently, it is essential to identify a lightweight LLM that balances low computational requirements with high accuracy and coherence in output generation. Through empirical evaluation, we found that Phi-3-mini-4k-instruct (Abdin et al. 2024) is both convenient to deploy and effective in producing consistently structured outputs. To assess the impact of the choice of LLM, we compared the performance of Phi-3 with LLaMA-3.1-8B-Instruct (Touvron et al. 2023) and DeepSeek-R1-Distill-Qwen-1.5B (Guo et al. 2025), as shown in Table 3.

**Model Capabilities on Diversify Image Generations:** Figure 3 illustrates qualitative results of the proposed method with Geneval benchmark. We evaluate the model on four sub categories. Namely, counting, spatial, color and size. We generate four samples for each prompt while each generation having different seed. First two rows illustrate the images generated with Attend and Excite with SDv2.1 base and last two rows shows images generated with proposed method. For each example, ground-truth prompt positioned at the top. Results of our model showcase the ability to bind attributes to respective objects while maintaining spatial consistency across the generated image.

## Limitations

Some failures can be attributed to the model’s tendency to interpret prompts in an overly literal manner. As shown in the first two columns of Table 5, these outputs were deemed incorrect, despite accurately reflecting a literal reading of the input descriptions. Despite the proposed model yielding superior performance, it struggles to accurately follow counting instructions when the quantity value increases to higher numbers, thereby resulting in deviations from the intended visual structure as shown in last three columns of Table 5. Such inconsistencies underscore the necessity of enhancing the model’s capacity to generalize across diverse aspects of visual composition.

## Conclusion and Future Work

In this work, we address a critical challenge in text-to-image synthesis: the accurate interpretation and visual representation of complex prompts involving multiple objects and intricate spatial relationships. Our proposed approach, grounded in scene graph structures, constitutes a substantial advancement over prior methods through the integration of the ASQL

Conditioner, which generates visual conditioning signals using a lightweight language model and directs the diffusion-based generation process via inference-time optimization. Through wide-ranging experiments, we demonstrate the capacity of our model. Consequently, future research directions should focus on augmenting the model’s architecture to improve its ability to accurately interpret and render complex compositional instructions, thereby bridging the gap between textual descriptions and their visual realizations.

## References

Abdin, M.; Aneja, J.; Awadalla, H.; Awadallah, A.; Awan, A. A.; Bach, N.; Bahree, A.; Bakhtiari, A.; Bao, J.; Behl, H.; et al. 2024. Phi-3 technical report: A highly capable language model locally on your phone. *arXiv preprint arXiv:2404.14219*.

Avrahami, O.; Hayes, T.; Gafni, O.; Gupta, S.; Taigman, Y.; Parikh, D.; Lischinski, D.; Fried, O.; and Yin, X. 2023. Spatext: Spatio-textual representation for controllable image generation. In *Proceedings of the IEEE/CVF Conference on Computer Vision and Pattern Recognition*, 18370–18380.

Bakr, E. M.; Sun, P.; Shen, X.; Khan, F. F.; Li, L. E.; and Elhoseiny, M. 2023. Hrs-bench: Holistic, reliable and scalable benchmark for text-to-image models. In *Proceedings of the IEEE/CVF International Conference on Computer Vision*, 20041–20053.

Balaji, Y.; Nah, S.; Huang, X.; Vahdat, A.; Song, J.; Kreis, K.; and Liu, M. 2022. Ediffi: Text-to-image diffusion models with an ensemble of expert denoisers. *arXiv* 2022. *arXiv preprint arXiv:2211.01324*.

Bansal, A.; Chu, H.-M.; Schwarzschild, A.; Sengupta, S.; Goldblum, M.; Geiping, J.; and Goldstein, T. 2023. Universal guidance for diffusion models. In *Proceedings of the IEEE/CVF Conference on Computer Vision and Pattern Recognition*, 843–852.

Beaumont, R. 2022. Clip Retrieval: Easily compute clip embeddings and build a clip retrieval system with them. <https://github.com/rom1504/clip-retrieval>.

Chefer, H.; Alaluf, Y.; Vinker, Y.; Wolf, L.; and Cohen-Or, D. 2023. Attend-and-excite: Attention-based semantic guidance for text-to-image diffusion models. *ACM Transactions on Graphics (TOG)*, 42(4): 1–10.

Chen, J.; Yu, J.; Ge, C.; Yao, L.; Xie, E.; Wu, Y.; Wang, Z.; Kwok, J.; Luo, P.; Lu, H.; and Li, Z. 2023. PixArt- $\alpha$ : Fast Training of Diffusion Transformer for Photorealistic Text-to-Image Synthesis. *arXiv:2310.00426*.

Chen, M.; Laina, I.; and Vedaldi, A. 2024. Training-free layout control with cross-attention guidance. In *Proceedings of the IEEE/CVF Winter Conference on Applications of Computer Vision*, 5343–5353.

Choi, W. S.; Heo, Y.-J.; and Zhang, B.-T. 2022. Sgram: Improving scene graph parsing via abstract meaning representation. *arXiv preprint arXiv:2210.08675*.

Dayma, B.; Patil, S.; Cuenca, P.; Saifullah, K.; Abraham, T.; Lê Khac, P.; Melas, L.; and Ghosh, R. 2021. DALL-E Mini.

Farshad, A.; Yeganeh, Y.; Chi, Y.; Shen, C.; Ommer, B.; and Navab, N. 2023. Scenegenie: Scene graph guided diffusion models for image synthesis. In *Proceedings of the IEEE/CVF International Conference on Computer Vision*, 88–98.

Feng, W.; He, X.; Fu, T.-J.; Jampani, V.; Akula, A.; Narayana, P.; Basu, S.; Wang, X. E.; and Wang, W. Y. 2022. Training-free structured diffusion guidance for compositional text-to-image synthesis. *arXiv preprint arXiv:2212.05032*.

Feng, W.; Zhu, W.; Fu, T.-J.; Jampani, V.; Akula, A.; He, X.; Basu, S.; Wang, X. E.; and Wang, W. Y. 2023. Layoutgpt: Compositional visual planning and generation with large language models. *Advances in Neural Information Processing Systems*, 36: 18225–18250.

Feng, Y.; Gong, B.; Chen, D.; Shen, Y.; Liu, Y.; and Zhou, J. 2024. Ranni: Taming text-to-image diffusion for accurate instruction following. In *Proceedings of the IEEE/CVF Conference on Computer Vision and Pattern Recognition*, 4744–4753.

Ghosh, D.; Hajishirzi, H.; and Schmidt, L. 2023. Geneval: An object-focused framework for evaluating text-to-image alignment. *Advances in Neural Information Processing Systems*, 36: 52132–52152.

Goodfellow, I.; Pouget-Abadie, J.; Mirza, M.; Xu, B.; Warde-Farley, D.; Ozair, S.; Courville, A.; and Bengio, Y. 2020. Generative adversarial networks. *Communications of the ACM*, 63(11): 139–144.

Guo, D.; Yang, D.; Zhang, H.; Song, J.; Zhang, R.; Xu, R.; Zhu, Q.; Ma, S.; Wang, P.; Bi, X.; et al. 2025. Deepseek-r1: Incentivizing reasoning capability in llms via reinforcement learning. *arXiv preprint arXiv:2501.12948*.

Herzig, R.; Bar, A.; Xu, H.; Chechik, G.; Darrell, T.; and Globerson, A. 2020. Learning canonical representations for scene graph to image generation. In *Computer Vision–ECCV 2020: 16th European Conference, Glasgow, UK, August 23–28, 2020, Proceedings, Part XXVI 16*, 210–227. Springer.

Ho, J. 2022. Classifier-Free Diffusion Guidance. *ArXiv*, abs/2207.12598.

Ho, J.; Jain, A.; and Abbeel, P. 2020. Denoising Diffusion Probabilistic Models. *arXiv preprint arXiv:2006.11239*.

Huang, C. T.; and Mitchell, O. R. 2002. A Euclidean distance transform using grayscale morphology decomposition. *IEEE Transactions on pattern analysis and machine intelligence*, 16(4): 443–448.

Huang, K.; Sun, K.; Xie, E.; Li, Z.; and Liu, X. 2023. T2i-compbench: A comprehensive benchmark for open-world compositional text-to-image generation. *Advances in Neural Information Processing Systems*, 36: 78723–78747.

Jiménez, Á. B. 2023. Mixture of diffusers for scene composition and high resolution image generation. *arXiv preprint arXiv:2302.02412*.

Johnson, J.; Gupta, A.; and Fei-Fei, L. 2018. Image generation from scene graphs. In *Proceedings of the IEEE conference on computer vision and pattern recognition*, 1219–1228.

Johnson, J.; Krishna, R.; Stark, M.; Li, L.-J.; Shamma, D.; Bernstein, M.; and Fei-Fei, L. 2015. Image retrieval using scene graphs. In *Proceedings of the IEEE conference on computer vision and pattern recognition*, 3668–3678.

Kim, Y.; Lee, J.; Kim, J.-H.; Ha, J.-W.; and Zhu, J.-Y. 2023. Dense text-to-image generation with attention modulation. In *Proceedings of the IEEE/CVF International Conference on Computer Vision*, 7701–7711.

Kingma, D. P.; and Welling, M. 2014. Auto-Encoding Variational Bayes. In *2nd International Conference on Learning Representations, ICLR 2014, Banff, AB, Canada, April 14–16, 2014, Conference Track Proceedings*.

Kumari, N.; Zhang, B.; Zhang, R.; Shechtman, E.; and Zhu, J.-Y. 2023. Multi-concept customization of text-to-image diffusion. In *Proceedings of the IEEE/CVF Conference on Computer Vision and Pattern Recognition*, 1931–1941.

Lambert, N.; Morrison, J.; Pyatkin, V.; Huang, S.; Iivison, H.; Brahman, F.; Miranda, L. J. V.; Liu, A.; Dziri, N.; Lyu, S.; Gu, Y.; Malik, S.; Graf, V.; Hwang, J. D.; Yang, J.; Bras, R. L.; Tafjord, O.; Wilhelm, C.; Soldaini, L.; Smith, N. A.; Wang, Y.; Dasigi, P.; and Hajishirzi, H. 2024. Tülu 3: Pushing Frontiers in Open Language Model Post-Training.

Li, J.; Li, D.; Savarese, S.; and Hoi, S. 2023a. Blip-2: Bootstrapping language-image pre-training with frozen image encoders and large language models. In *International conference on machine learning*, 19730–19742. PMLR.

Li, Y.; Liu, H.; Wu, Q.; Mu, F.; Yang, J.; Gao, J.; Li, C.; and Lee, Y. J. 2023b. GLIGEN: Open-Set Grounded Text-to-Image Generation. *CVPR*.

Li, Z.; Chai, Y.; Zhuo, T. Y.; Qu, L.; Haffari, G.; Li, F.; Ji, D.; and Tran, Q. H. 2023c. FACTUAL: A Benchmark for Faithful and Consistent Textual Scene Graph Parsing. In *Findings of the Association for Computational Linguistics: ACL 2023*, 6377–6390. Toronto, Canada: Association for Computational Linguistics.

Liu, N.; Li, S.; Du, Y.; Torralba, A.; and Tenenbaum, J. B. 2022. Compositional visual generation with composable diffusion models. In *European Conference on Computer Vision*, 423–439. Springer.

Nichol, A. Q.; Dhariwal, P.; Ramesh, A.; Shyam, P.; Mishkin, P.; McGrew, B.; Sutskever, I.; and Chen, M. 2022. GLIDE: Towards Photorealistic Image Generation and Editing with Text-Guided Diffusion Models. In Chaudhuri, K.; Jegelka, S.; Song, L.; Szepesvari, C.; Niu, G.; and Sabato, S., eds., *Proceedings of the 39th International Conference on Machine Learning*, volume 162 of *Proceedings of Machine Learning Research*, 16784–16804. PMLR.

Peebles, W.; and Xie, S. 2023. Scalable diffusion models with transformers. In *Proceedings of the IEEE/CVF international conference on computer vision*, 4195–4205.

Pham, K.; Huynh, C.; Lim, S.-N.; and Shrivastava, A. 2024. Composing object relations and attributes for image-text matching. In *Proceedings of the IEEE/CVF Conference on Computer Vision and Pattern Recognition*, 14354–14363.

Phung, Q.; Ge, S.; and Huang, J.-B. 2024. Grounded text-to-image synthesis with attention refocusing. In *Proceedings of the IEEE/CVF Conference on Computer Vision and Pattern Recognition*, 7932–7942.

Radford, A.; Kim, J. W.; Hallacy, C.; Ramesh, A.; Goh, G.; Agarwal, S.; Sastry, G.; Askell, A.; Mishkin, P.; Clark, J.; et al. 2021. Learning transferable visual models from natural language supervision. In *International conference on machine learning*, 8748–8763. PMLR.

Ramesh, A.; Dhariwal, P.; Nichol, A.; Chu, C.; and Chen, M. 2022a. Hierarchical text-conditional image generation with clip latents. *arXiv preprint arXiv:2204.06125*, 1(2): 3.

Ramesh, A.; Dhariwal, P.; Nichol, A.; Chu, C.; and Chen, M. 2022b. Hierarchical Text-Conditional Image Generation with CLIP Latents. *ArXiv*, abs/2204.06125.

Rombach, R.; Blattmann, A.; Lorenz, D.; Esser, P.; and Ommer, B. 2021. High-Resolution Image Synthesis with Latent Diffusion Models. *arXiv:2112.10752*.

Rombach, R.; Blattmann, A.; Lorenz, D.; Esser, P.; and Ommer, B. 2022. High-resolution image synthesis with latent diffusion models. In *Proceedings of the IEEE/CVF conference on computer vision and pattern recognition*, 10684–10695.

Saharia, C.; Chan, W.; Saxena, S.; Li, L.; Whang, J.; Denton, E. L.; Ghasemipour, K.; Gontijo Lopes, R.; Karagol Ayan, B.; Salimans, T.; et al. 2022. Photorealistic text-to-image diffusion models with deep language understanding. *Advances in neural information processing systems*, 35: 36479–36494.

Schuster, S.; Krishna, R.; Chang, A.; Fei-Fei, L.; and Manning, C. D. 2015. Generating semantically precise scene graphs from textual descriptions for improved image retrieval. In *Proceedings of the fourth workshop on vision and language*, 70–80.

Shen, G.; Wang, L.; Lin, J.; Ge, W.; Zhang, C.; Tao, X.; Zhang, Y.; Wan, P.; Wang, Z.; Chen, G.; et al. 2024. Sg-adapter: Enhancing text-to-image generation with scene graph guidance. *arXiv preprint arXiv:2405.15321*.

Song, Y.; Sohl-Dickstein, J.; Kingma, D. P.; Kumar, A.; Ermon, S.; and Poole, B. 2021. Score-Based Generative Modeling through Stochastic Differential Equations. In *International Conference on Learning Representations*.

Sudre, C. H.; Li, W.; Vercauteren, T.; Ourselin, S.; and Jorge Cardoso, M. 2017. Generalised dice overlap as a deep learning loss function for highly unbalanced segmentations. In *International Workshop on Deep Learning in Medical Image Analysis*, 240–248. Springer.

Sueyoshi, K.; and Matsubara, T. 2024. Predicated diffusion: Predicate logic-based attention guidance for text-to-image diffusion models. In *Proceedings of the IEEE/CVF Conference on Computer Vision and Pattern Recognition*, 8651–8660.

Tong, S.; Jones, E.; and Steinhhardt, J. 2024. Mass-producing failures of multimodal systems with language models. *Advances in Neural Information Processing Systems*, 36.

Tong, S.; Liu, Z.; Zhai, Y.; Ma, Y.; LeCun, Y.; and Xie, S. 2024. Eyes wide shut? exploring the visual shortcomings of multimodal llms. In *Proceedings of the IEEE/CVF Conference on Computer Vision and Pattern Recognition*, 9568–9578.

Touvron, H.; Lavril, T.; Izacard, G.; Martinet, X.; Lachaux, M.-A.; Lacroix, T.; Rozière, B.; Goyal, N.; Hambro, E.; Azhar, F.; et al. 2023. Llama: Open and efficient foundation language models. *arXiv preprint arXiv:2302.13971*.

Wang, D.; Beck, D.; and Cohn, T. 2019. On the Role of Scene Graphs in Image Captioning. In Mogadala, A.; Klakow, D.; Pezzelle, S.; and Moens, M.-F., eds., *Proceedings of the Beyond Vision and LANguage: inTEgrating Real-world kNowledge (LANTERN)*, 29–34. Hong Kong, China: Association for Computational Linguistics.

Wang, Y.; Li, Z.; Zhang, W.; Zhang, Z.; Xie, B.; Liu, X.; Zeng, W.; and Jin, X. 2024. Scene graph disentanglement and composition for generalizable complex image generation. *Advances in Neural Information Processing Systems*, 37: 98478–98504.

Wei, J.; Wang, X.; Schuurmans, D.; Bosma, M.; Xia, F.; Chi, E.; Le, Q. V.; Zhou, D.; et al. 2022. Chain-of-thought prompting elicits reasoning in large language models. *Advances in neural information processing systems*, 35: 24824–24837.

Wu, S.; Fei, H.; Zhang, H.; and Chua, T.-S. 2023. Imagine that! abstract-to-intricate text-to-image synthesis with scene graph hallucination diffusion. *Advances in Neural Information Processing Systems*, 36: 79240–79259.

Xu, B.; Yan, Q.; Liao, R.; Wang, L.; and Sigal, L. 2024a. Joint generative modeling of scene graphs and images via diffusion models. *arXiv preprint arXiv:2401.01130*.

Xu, L.; Zhao, S.; Lin, Q.; Chen, L.; Luo, Q.; Wu, S.; Ye, X.; Feng, H.; and Du, Z. 2024b. Evaluating Large Language Models on Spatial Tasks: A Multi-Task Benchmarking Study. *arXiv preprint arXiv:2408.14438*.

Yamada, Y.; Bao, Y.; Lampinen, A. K.; Kasai, J.; and Yildirim, I. 2023. Evaluating spatial understanding of large language models. *arXiv preprint arXiv:2310.14540*.

Yang, X.; Peng, J.; Wang, Z.; Xu, H.; Ye, Q.; Li, C.; Huang, S.; Huang, F.; Li, Z.; and Zhang, Y. 2023. Transforming visual scene graphs to image captions. *arXiv preprint arXiv:2305.02177*.

Yuksekgonul, M.; Bianchi, F.; Kalluri, P.; Jurafsky, D.; and Zou, J. 2022. When and why vision-language models behave like bags-of-words, and what to do about it? *arXiv preprint arXiv:2210.01936*.

Zhang, Y.; Yu, P.; and Wu, Y. N. 2024. Object-conditioned energy-based attention map alignment in text-to-image diffusion models. In *European Conference on Computer Vision*, 55–71. Springer.

Zhong, Y.; Shi, J.; Yang, J.; Xu, C.; and Li, Y. 2021. Learning to generate scene graph from natural language supervision. In *Proceedings of the IEEE/CVF International Conference on Computer Vision*, 1823–1834.